Inorganic Chemistry

Article

pubs.acs.org/IC

# pH Controlled Pathway and Systematic Hydrothermal Phase Diagram for Elaboration of Synthetic Lead Nickel Selenites

Vadim M. Kovrugin,[†,‡] Marie Colmont,[†] Christine Terryn,[§] Silviu Colis,[∥] Oleg I. Siidra,[‡] Sergey V. Krivovichev,[‡] and Olivier Mentré*[,†]

[†]Université Lille Nord de France, UMR 8181 CNRS, Unité de Catalyse et de Chimie du Solide (UCCS USTL), 59655 Villeneuve d'ASCQ, France

[‡]Department of Crystallography, Saint-Petersburg State University, Universitetskaya nab. 7/9, 199034 St. Petersburg, Russia

[§]Plateforme Imagerie Cellulaire et Tissulaire, 51 rue Cognacq-Jay, 51100 Reims, France

[∥]Institut de Physique et Chimie des Matériaux de Strasbourg (IPCMS), UMR 7504 CNRS and Université de Strasbourg (UDS-ECPM), F-67034 Cedex 2 Strasbourg, France

Supporting Information

**ABSTRACT:** The PbO−NiO−$SeO_2$ ternary system was fully studied using constant hydrothermal conditions at 473 K. It yields the establishment of the corresponding phase diagram using a systematic assignment of reaction products by both powder and single-crystal X-ray diffraction. It leads to the preparation of three novel lead nickel selenites, $\alpha$-$PbNi(SeO_3)_2$ (**I**), $\beta$-$PbNi(SeO_3)_2$ (**II**), and $PbNi_2(SeO_2OH)_2(SeO_3)_2$ (**III**), and one novel lead cobalt selenite, $\alpha$-$PbCo(SeO_3)_2$ (**IV**), which have been structurally characterized. The crystal structures of the $\alpha$-forms **I**, **IV**, and **III** are based on a 3D complex nickel selenite frameworks, whereas the $\beta$-$PbNi(SeO_3)_2$ modification (**II**) consists of nickel selenite sheets stacked in a noncentrosymmetric structure, second-harmonic generation active. The pH value of the starting solution was shown to play an essential role in the reactive processes. Magnetic measurements of **I**, **III**, and **IV** are discussed.

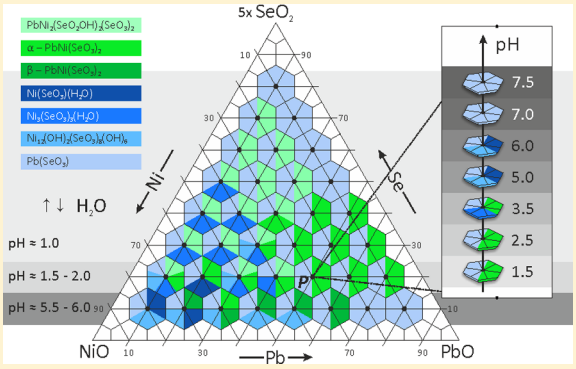


## INTRODUCTION

The demand for specific noncentrosymmetric (NCS) crystal structures is very strong because interesting physical properties, such as second-harmonic generation (SHG),[1] piezoelectricity,[2] ferroelectricity,[3] and pyroelectricity,[4] can be expected. In particular, nonlinear optic materials have become tremendously important and are drawing more and more attention owing to their promising applications in laser science and technology. The NCS compounds are commonly observed when dealing with ($Ti^{4+}$, $V^{5+}$, $Mo^{6+}$) octahedrally coordinated $d^0$ transition metals susceptible to second-order Jahn−Teller (SOJT) effects. Typical SOJT asymmetric coordination environments are also favored for cations with a stereoactive lone pair of electrons ($As^{3+}$, $Se^{4+}$, $Sb^{3+}$, $Pb^{2+}$, and $Bi^{3+}$, etc.) in more drastic manner leading to a diversity of unusual polyhedral coordination. The crystal chemistry of metal selenites is very rich as first reviewed by Verma.[5] The incorporation of heavy lone pair cations such as $Pb^{2+}/Bi^{3+}$ with selenite groups increases the chance to achieve asymmetric building units or NCS crystal structures as demonstrated in several earlier works dedicated to the exploration of $PbO/Bi_2O_3$−$MO_x$−$SeO_2$ (M = $Cu^{2+}$, $V^{3+}$, $Ge^{4+}$, $Nb^{5+}$, $V^{5+}$, $Mo^{6+}$, $W^{6+}$; $x$ = 1, 2; $y$ = 1, 2, 3, 5) ternary systems.[6−11] From the experimental viewpoint, due to the low and close melting and sublimation temperatures (340 and 350 °C, respectively), the crystal growth of selenites is generally achieved using either chemical transport routes,[12,13] recently leading to original bismuth selenites, including giant cell compounds,[14] or hydrothermal methods due to the good solubility and reactivity of $(SeO_3)^{2-}$ anions. However, as recently demonstrated by the evidence of a number of phases in competition in the $CoSeO_3$−$SeO_2$−$H_2O$ phase diagram[15] and other hybrid inorganic−organic systems,[16,17] a systematic approach may be preferred for exhaustive search of novel crystal structures. Thus, research was not yet carried out on ternary systems with lead and nickel/cobalt as transition metals constituents. Herein, we present a scrupulous investigation of the PbO−NiO−$SeO_2$ system in hydrothermal conditions. It leads to the synthesis of four novel lead selenites, $\alpha$-$PbNi(SeO_3)_2$ (**I**), $\beta$-$PbNi(SeO_3)_2$ (**II**), $PbNi_2(SeO_2OH)_2(SeO_3)_2$ (**III**), and $\alpha$-$PbCo(SeO_3)_2$ (**IV**), that have been structurally characterized by single-crystal X-ray diffraction (XRD). Their magnetic properties will be also discussed in this Article.

**Received:** December 22, 2014
**Published:** February 17, 2015





DOI: 10.1021/ic503055v
*Inorg. Chem.* 2015, 54, 2425−2434

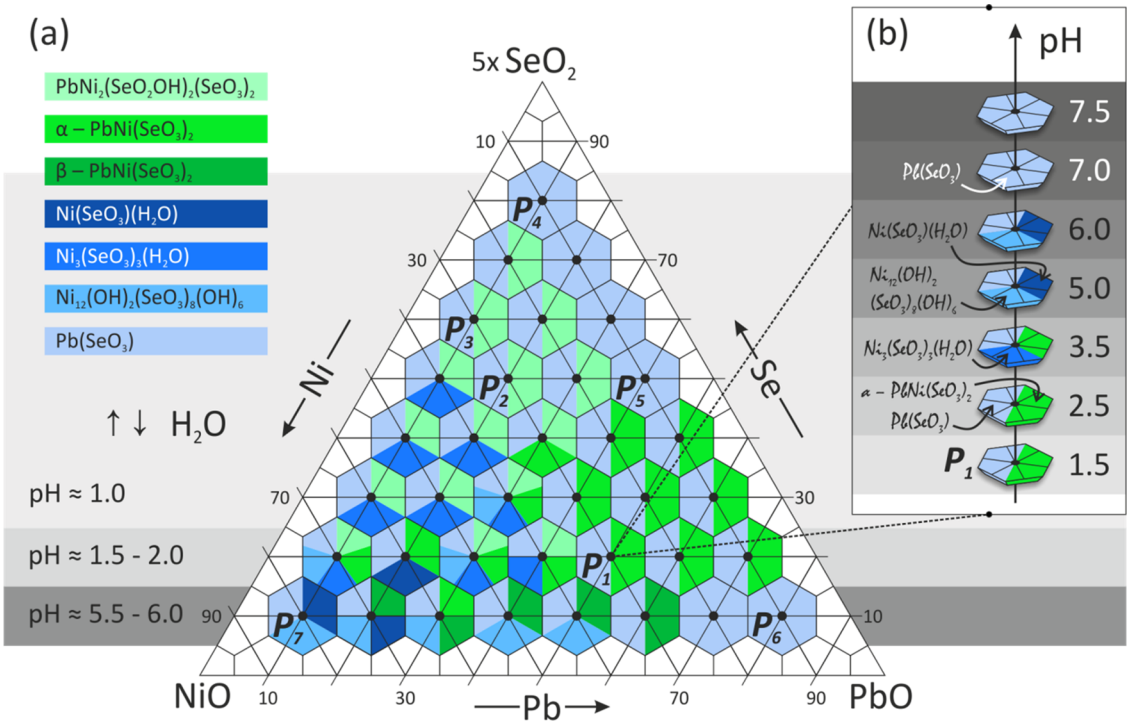


**Figure 1.** Experimental crystallization diagram of the PbO–NiO–$SeO_2$–$H_2O$ system at 423 K with the pH zones shown in the background by gray colors (a), and the series of experiments with a PbO:NiO:$SeO_2$ molar ratio of 5:3:10 corresponding to the $P_1$ point with various pH values (b). The black points indicate the experimental combinations of the molar ratios of precursors. The compositions of various phases synthesized in each experimental point are shown by hexagons of different colors..

**Table 1. Crystallographic Data for the compounds $\alpha$- $PbNi(SeO_3)_2$ (I), $\beta$-$PbNi(SeO_3)_2$ (II), $PbNi_2(SeO_2OH)_2(SeO_3)_2$ (III), and $\alpha$-$PbCo(SeO_3)_2$ (IV)**

| | I | II | III | IV |
|---|---|---|---|---|
| $M_r$ (g $mol^{-1}$) | 519.82 | 519.82 | 834.47 | 520.04 |
| cryst syst | orthorhombic | orthorhombic | monoclinic | orthorhombic |
| space group | *Pnma* | $Cmc2_1$ | *P2/c* | *Pnma* |
| *a* (Å) | 12.7476(4) | 5.4715(4) | 13.6824(10) | 12.8208(4) |
| *b* (Å) | 5.4562(2) | 9.1963(6) | 5.2692(5) | 5.4902(2) |
| *c* (Å) | 7.8332(2) | 11.4436(9) | 19.3476(13) | 7.9085(2) |
| $\alpha$ (deg) | 90 | 90 | 90 | 90 |
| $\beta$ (deg) | 90 | 90 | 129.524(4) | 90 |
| $\gamma$ (deg) | 90 | 90 | 90 | 90 |
| *V* ($Å^3$) | 544.83(3) | 575.81(7) | 1075.94 (16) | 556.67(3) |
| *Z* | 4 | 4 | 4 | 4 |
| $\rho$ ($g/cm^3$) | 6.337 | 5.996 | 5.151 | 6.205 |
| $\mu$ ($mm^{-1}$) | 47.637 | 45.074 | 32.668 | 46.221 |
| $\lambda$(Mo K$\alpha$) (Å) | 0.71073 | 0.71073 | 0.71073 | 0.71073 |
| $\theta_{min-max}$ (deg) | 3.1–29.6 | 3.6–28.0 | 1.9–28.0 | 3.0–28.0 |
| reflns collected | 10212 | 2345 | 5454 | 3226 |
| indep reflns ($R_{int}$) | 823 (0.0336) | 686 (0.0260) | 2083 (0.0459) | 742 (0.0260) |
| $R_1$ ($I > 2\sigma(I)$) | 0.0139 | 0.0141 | 0.0496 | 0.0186 |
| $wR_2$ ($I > 2\sigma(I)$) | 0.0360 | 0.0346 | 0.0992 | 0.0429 |
| $R_1$ (all data) | 0.0165 | 0.0142 | 0.0783 | 0.0203 |
| $wR_2$ (all data) | 0.0387 | 0.0346 | 0.1104 | 0.0439 |
| GOF | 1.090 | 1.109 | 1.187 | 1.142 |
| $\Delta\rho_{max}/\Delta\rho_{min}$ (e $Å^{-3}$) | 1.573/−1.110 | 1.310/−1.073 | 2.916/−2.912 | 0.971/−1.887 |

## EXPERIMENTAL SECTION

**Syntheses.** Commercial PbO (99,999%, Aldrich), $SeO_2$ (99%, Alfa Aesar), NiO (99%, Sigma-Aldrich), and CoO (95%, Alfa Aesar) were used as received. After weighing and grinding, the reagents were mixed in 6 mL of distilled water. When necessary, sodium hydroxide solution was used to adjust the pH to its desired value. Our exploration of the crystal growth in the PbO–NiO–$SeO_2$–$H_2O$ system consisted of examination of 36 possible combinations of molar ratios of the solid precursors within the Gibbs's triangle (Figure 1a). In all syntheses the $m$PbO + $n$NiO + $(k/5)SeO_2$ ($m$, $n$, $k$ = 1, 2, ..., 8) molar sum was fixed as constant equal to 10 mmol, and the mixture was completed with 6 mL of



DOI: 10.1021/ic503055v
*Inorg. Chem.* 2015, 54, 2425–2434

distilled water. It has been experimentally established that only acidic conditions favor the crystallization of structural varieties. In our study, the reactive medium self-acidifies by solubilization of $SeO_2$ into selenous acid according to the following reactions:

$$SeO_2 + H_2O \rightarrow H_2SeO_3 \quad (1)$$

$$H_2SeO_3 \leftrightarrow H^+ + (HSeO_3)^- \quad (pK_a = 2.62) \quad (2)$$

$$(HSeO_3)^- \leftrightarrow H^+ + (SeO_3)^{2-} \quad (pK_a = 8.32) \quad (3)$$

Then a large stoichiometric excess of $SeO_2$ was necessary to achieve reactions as shown in Figure 1a, where the amount of selenium dioxide is multiplied by five. The pH values increase from ∼1 to ∼5.5−6.0 on decreasing the $SeO_2$ content in our experimental range. The solid products were systematically analyzed by powder XRD (PXRD) analysis (after grinding), while representative crystals of each of the present phases were also selected by morphology and colors and tested by single-crystal XRD analysis. It leads to the phase distribution given in Figure 1a, where the crystallization domains of phases are illustrated by different colors.

The chemical reactions were performed during 36 h in 23 mL Teflon-lined Parr reaction vessels heated in an oven at 473 K. At the end of the experiment time, the vessels were cooled during 48 h. The precipitate was filtered through filter paper. Single crystals of three novel lead selenites with nickel, $\alpha$-$PbNi(SeO_3)_2$ (**I**), $\beta$-$PbNi(SeO_3)_2$ (**II**), and $PbNi_2(SeO_2OH)_2(SeO_3)_2$ (**III**), have been prepared by the hydrothermal techniques. They have been observed in the mixtures already reported: $Ni(SeO_3)(H_2O)$,[18] $Ni_3(SeO_2)_3(H_2O)$,[19,20] $Ni_{12}(OH)_6(SeO_3)_8(OH)_2$,[21] and $Pb(SeO_3)$.[22−25] Single crystals of the cobalt selenite, $\alpha$-$PbCo(SeO_3)_2$ (**IV**) were obtained by the reaction analogous to that used to obtain compound **I**. Attempts to synthesize the Co analogue of compounds **II** and **III** using similar techniques proved unsuccessful. In general, out of **IV** our hydrothermal conditions using cobalt precursors rarely lead to crystal growth, which is one motivation of our study. The novel lead selenite crystals occur as yellow needles (**I**), yellow prisms (**II**), green plates (**III**), and purple needles (**IV**) up to 300 $\mu$m in maximal dimension.

**X-ray Diffraction.** Powder X-ray diffraction analyses of all of the powder samples were performed at room temperature in a $2\theta$ range of 10−60° with a scan step width of 0.02° using a D8 Advance Bruker AXS diffractometer (Cu K$\alpha$ radiation, $\lambda$ = 1.5418 Å). Single crystals selected for data collection were examined under an optical microscope and mounted on a glass fiber. Data were collected by means of a Bruker DUO four-circle diffractometer equipped with an APEX II CCD detector and monochromated Mo K$\alpha$ radiation. Unit-cell parameters were refined by the least-squares techniques using the full recorded data set. The data were integrated and corrected for absorption using a multiscan type model implemented in the Bruker programs APEX[26] and SADABS.[27] The structures were solved by direct methods and refined by means of the program SHELXL-2013.[28] Crystallographic data are summarized in Table 1. The visible difference in the quality of the crystallographic data of compound **III** is a result of the relatively poor quality and small size of the collected crystal. Fractional atomic coordinates, atomic displacement parameters, and selected bond distances are listed in Tables S1−S12 of the Supporting Information. The crystal structure data for $\alpha$-$PbCo(SeO_3)_2$, $\alpha$-$PbNi(SeO_3)_2$, $\beta$-$PbNi(SeO_3)_2$, and $PbNi_2(SeO_2OH)_2(SeO_3)_2$ were deposited with the depository numbers CSD-428904, CSD-428905, CSD-428906, and CSD-428907, respectively.

**SQUID.** The magnetic properties of the samples were analyzed using a MPMS SQUID-VSM (Quantum Design) magnetometer in a temperature and field range of 1.8−300 K and 0−7 T, respectively. The temperature dependence variation of the magnetization was carried out under a magnetic field of 0.1 T after cooling the sample in a field of 0.1 T (FC, field cooling) or in zero field (ZFC, zero-field cooling). Using these variations, $\chi$ and $\chi^{-1}$ vs $T$ could be obtained that could inform on the magnetic interactions. All measurements were carried out on nonaligned samples (random crystallites orientation).

**Multiphoton SHG Microscopy.** For compound **II**, a laser scanning microscope LSM 710 NLO Zeiss (Jena, Germany) was used as implemented at the Plateforme d'Imagerie Cellulaire et Tissulaire, Reims, France. Excitation was provided by a CHAMELEON femtosecond titanium−sapphire laser (Coherent, Santa Clara, CA, USA) set at 860 nm, tuning the power until SHG was detected. Samples were imaged with a 20× , 0.8 NA objective lens. The emitted signal of SHG was collected with a bandpass filter (420−440 nm). The analyzed zone is performed by pixels of 0.55 × 0.55 $\mu m^2$.

**Partial Charge and Dipole Moment Calculations.** We have chosen to follow Henrýs model for determination of partial charges using scales of atomic nonempirical electronegativity and hardness (to measure the resistance the atom can oppose to the flow of electronic density) implemented in the program PACHA. This software uses a nonempirical method to determine partial charges using crystal structure data and two parameters per chemical element: configuration energy and the radius of the most diffuse valence orbital to avoid any unphysical aspects.[29]

## RESULTS AND DISCUSSION

**Phases in Competition.** The analysis of the different solid phases in competition allows a rough rationalization on the basis of the starting stoichiometry and pH value. First, we note that the $Pb(SeO_3)$ compound is the most frequent phase in the system, and it has been observed as a solid product with variable degree of

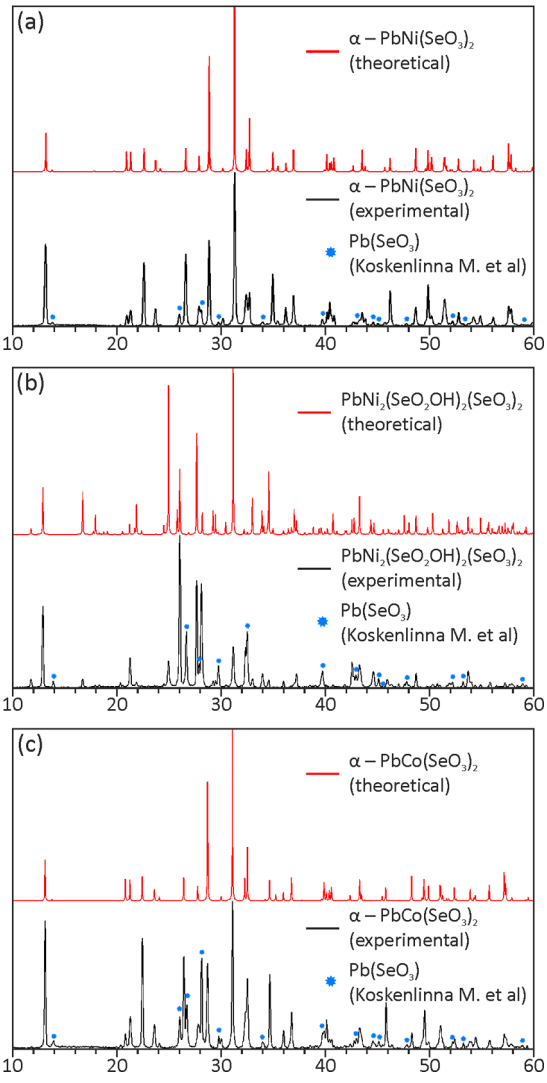


**Figure 2.** Theoretical (red) and experimental (black) PXRD patterns for the crystal structures of $\alpha$-$PbNi(SeO_3)_2$ (a), $PbNi_2(SeO_2OH)_2(SeO_3)_2$ (b), and $\alpha$-$PbCo(SeO_3)_2$ (c).



DOI: 10.1021/ic503055v
Inorg. Chem. 2015, 54, 2425−2434

Table 2. Solid Products of the Experiments with a PbO/NiO/$SeO_2$ Molar Ratio of 5:3:10 (Point $P_1$ in Figure 1a)

| | pH | | |
|---|---|---|---|
| no. | before reaction | after reaction | solid products |
| $P_1$ | 1.0 | 1.5 | $Pb(SeO_3)$; $\alpha$-$PbNi(SeO_3)_2$ (**I**) |
| 1 | 1.5 | 2.5 | $Pb(SeO_3)$; $\alpha$-$PbNi(SeO_3)_2$ (**I**) |
| 2 | 2.0 | 3.5 | $Pb(SeO_3)$; $\alpha$-$PbNi(SeO_3)_2$ (**I**); $Ni_3(SeO_3)_3(H_2O)$ |
| 3 | 3.0 | 5.0 | $Pb(SeO_3)$; $Ni(SeO_3)(H_2O)$; $Ni_{12}(OH)_6(SeO_3)_8(OH)_2$ |
| 4 | 4.0 | 6.0 | $Pb(SeO_3)$; $Ni(SeO_3)(H_2O)$; $Ni_{12}(OH)_6(SeO_3)_8(OH)_2$ |
| 5 | 5.0 | 7.0 | $Pb(SeO_3)$ |
| 6 | 6.0 | 7.5 | $Pb(SeO_3)$ |

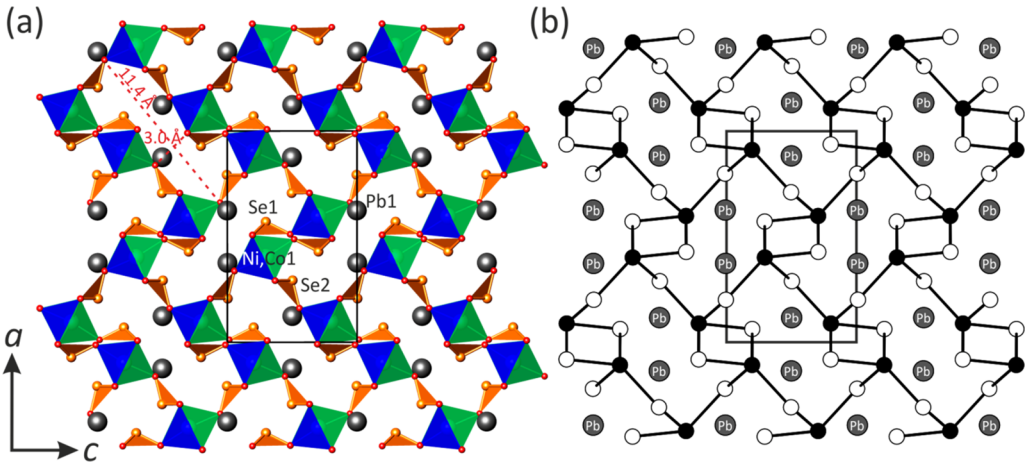


**Figure 3.** General projection of the crystal structures of $\alpha$-$PbM(SeO_3)_2$ (M = $Ni^{2+}$ (**I**), $Co^{2+}$ (**IV**)) along the *b* axis (a) and the corresponding black-and-white graph (b). Legend, panel a: $MO_6$ octahedra, blue-green; $SeO_3$ trigonal pyramids, orange; $Pb^{2+}$, gray balls. Legend panel b: $M^{2+}$, black circles; $Se^{4+}$, white circles.

crystallinity in each hydrothermal experiment, sometimes found as a predominant white powder. This proves a preferred complexation of $Pb^{2+}$ by $(SeO_3)^{2-}$ and enhanced precipitation independently of the pH. Second, about the cationic stoichiometry, rich lead compounds appear in the right zone of the diagram while lead-free nickel selenites ($Ni(SeO_3)(H_2O)$[18] and $Ni_3(SeO_2)_3(H_2O)$[19,20]) have been obtained at the left side with low Pb concentrations. This result, even though expected, demonstrates formation mechanisms controlled by the solution concentrations of each species. Finally, occulting the systematic presence of $Pb(SeO_3)$,[22−25] low pH values favor reactivity of $(HSeO_3)^-$ groups (e.g., in $PbNi_2(SeO_2OH)_2(SeO_3)_2$), while selenite groups predominate at higher pH values (e.g., $PbNi(SeO_3)$ polymorphs) in good agreement with the acidic reactions and p$K_a$s given earlier (eqs 2 and 3).

Experimental (black) and theoretical (red) PXRD patterns for new phases described later, $\alpha$-$PbNi(SeO_3)_2$ (**I**), $PbNi_2(SeO_2OH)_2(SeO_3)_2$ (**III**), and $\alpha$-$PbCo(SeO_3)_2$ (**IV**), are represented in Figure 2, leading to a mixture with diamagnetic $Pb(SeO_3)$. It enables the measurement of their magnetic properties. Intensities of the reflections in the PXRD patterns are affected by relatively strong preferred orientation, due to anisotropic crystallite shape related to the crystal structures. . Theoretical patterns were generated with PowderCell 2.4 from the single-crystal data without taking into account the preferred orientation. The PXRD patterns of **I** and **III** correspond to the samples performed for the $P_1$ point (PbO:NiO:$SeO_2$ = 5:3:10) and $P_2$ point (PbO:NiO:$SeO_2$ = 2:3:25) of Figure 1a, respectively. The solid products of **IV** for the powder X-ray diffraction analysis have been obtained with stoichiometry to analogous **I** by replacing NiO by CoO. For other stoichiometries, PXRD patterns corresponding to the $P_3$, $P_4$, $P_5$, $P_6$, and $P_7$ points in Figure 1a are provided as examples in the Supporting Information (Figures S1−S5).

**Influence of the pH.** To gain more information about the reaction processes in the PbO−NiO−$SeO_2$−$H_2O$ phase diagram, an in-depth investigation was carried out for the particular $P_1$ (PbO:NiO:$SeO_2$ molar ratio of 5:3:10) stoichiometric mixture at various pH values up to 7.5 (in order to prevent the reduction of $SeO_2$ to $\gamma$-Se metal[30,31]). The reagents were mixed with 1.75 M aqueous NaOH solution until the required pH values. Then, the hydrothermal treatment was applied. The resulted products of these series as a function of the pH values are listed in Table 2 and shown in Figure 1b. Experimental PXRD patterns are provided in the Supporting Information (Figures S6−S11).

The results obtained in the course of the hydrothermal experiments demonstrated an essential role of the pH values, especially dealing with the influence of the degree of condensation of the ionic species. Once more at all pH the $Pb(SeO_3)$ is revealed as very stable. For the other products, we observe that water molecules and, subsequently, hydroxide anions are progressively incorporated into the compound structures on increasing the pH. In particular, at low pH of 1.5−2.5 only condensed compounds, $\alpha$-$PbNi(SeO_3)_2$ (**I**) and $Pb(SeO_3)$,[22−25] are formed. The reaction occurring with pH value of 3.5 leads to reported compound $Ni_3(SeO_3)_3(H_2O)$[20] with one-third of $Ni^{2+}$ coordinated by water molecules. Increasing the pH to 5.0−6.0 markedly increases the incorporation of water molecules and/or hydroxyl groups leading to $Ni_{12}(OH)_2(SeO_3)_8(OH)_6$[21] and $Ni(SeO_3)(H_2O)$.[18] The crystal structure of the latter is only composed of


DOI: 10.1021/ic503055v
*Inorg. Chem.* 2015, 54, 2425−2434

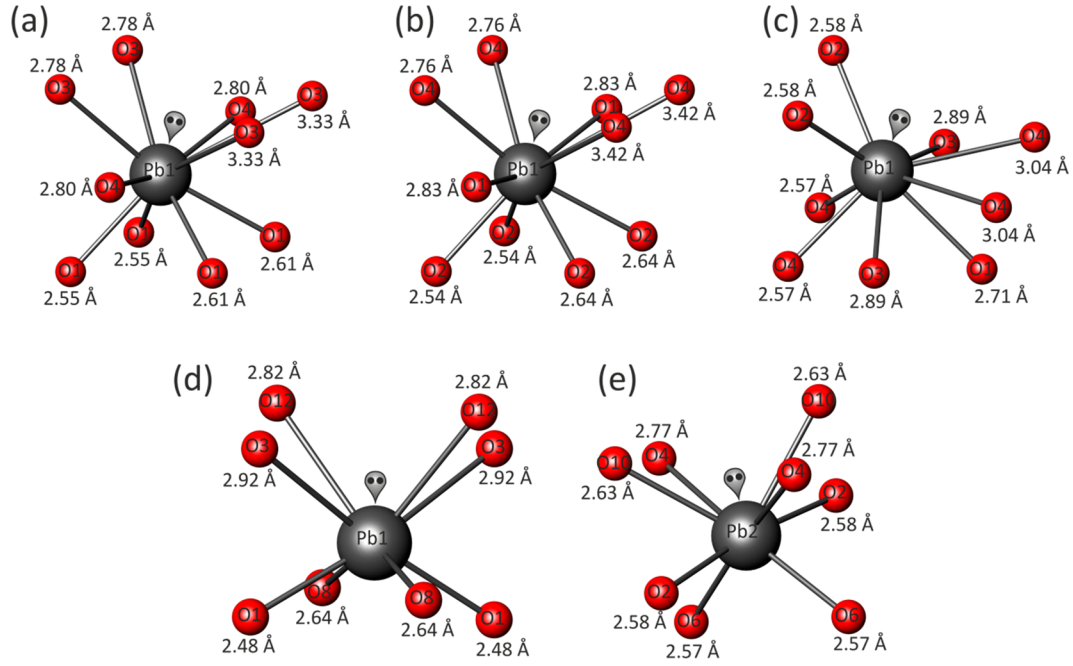


**Figure 4.** Coordination environment of $Pb^{2+}$ cations in the crystal structures of **I** (a), **IV** (b), **II** (c), and **III** (d and e).

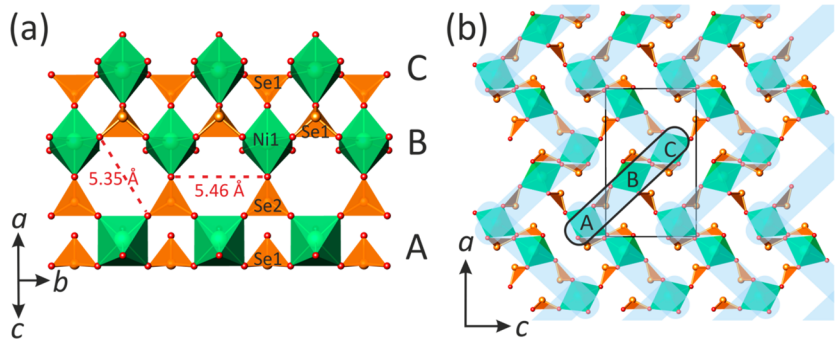


**Figure 5.** Polyhedral representation of the channel walls in $\alpha$-$PbNi(SeO_3)_2$ (a) and its projection along the *b* axis as a combination of the pseudoribbons cross-linked into a 3D framework ($Pb^{2+}$ cations are omitted for clarity) (b). Legend: $NiO_6$ octahedra, green; $SeO_3$ trigonal pyramids, orange.

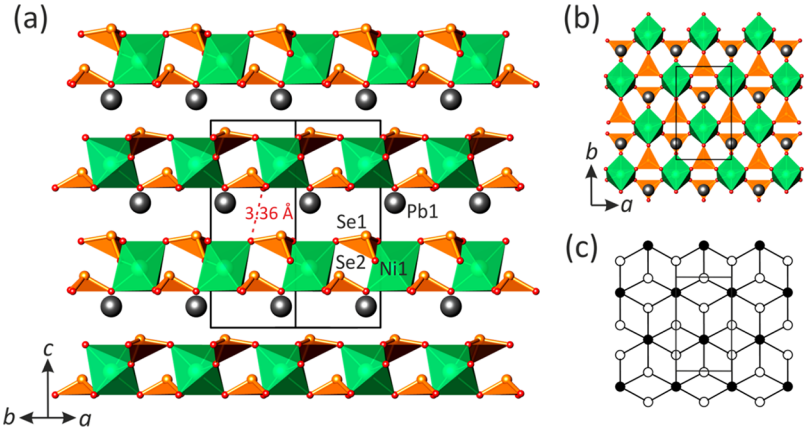


**Figure 6.** Crystal structure of $\beta$-$PbNi(SeO_3)_2$ in two different projections (a and b), and the black-and-white graph corresponding to the Ni−Se sheet in the structure ($Pb^{2+}$ cations are omitted for clarity) (c). Designations as in Figure 4.

$NiO_5(H_2O)$ polyhedra, while the tubular crystal structure of $Ni_{12}(OH)_2(SeO_3)_8(OH)_6$[21] contains half of the protonated $(NiO_5(OH))^{9-}$ octahedra. With pH values greater than 7.0, only the very stable solid products $Pb(SeO_3)^{22-25}$ phase is observed.

## STRUCTURAL DESCRIPTION

**$\alpha$-$PbM(SeO_3)_2$ (M = $Ni^{2+}$, $Co^{2+}$).** The isotypic compounds **I** and **IV** crystallize in orthorhombic symmetry (space group *Pnma*). They are built up from a 3D framework composed of



DOI: 10.1021/ic503055v
*Inorg. Chem.* 2015, 54, 2425−2434

**Table 3. Calculated Partial Charges for I ($\alpha$-$PbNi(SeO_3)_2$), II ($\beta$-$PbNi(SeO_3)_2$), III ($PbNi_2(SeO_2OH)_2(SeO_3)_2$), and IV ($\alpha$-$PbCo(SeO_3)_2$)**

| $\alpha$-$PbNi(SeO_3)_2$ | |
|---|---|
| atom | charge ± $q$ |
| Pb1 | +0.74952 |
| Se1 | +0.24784 |
| Se2 | +0.24417 |
| Ni1 | +0.93022 |
| O1 | −0.37204 |
| O2 | −0.33946 |
| O3 | −0.36119 |
| O4 | −0.36583 |

| $\beta$-$PbNi(SeO_3)_2$ | |
|---|---|
| atom | charge ± $q$ |
| Pb1 | +0.77033 |
| Se1 | +0.25253 |
| Se2 | +0.22790 |
| Ni1 | +0.90996 |
| O1 | −0.35484 |
| O2 | −0.35920 |
| O3 | −0.35784 |
| O4 | −0.36482 |

| $\alpha$-$PbCo(SeO_3)_2$ | |
|---|---|
| atom | charge ± $q$ |
| Pb1 | +0.73096 |
| Se1 | +0.23494 |
| Se2 | +0.23527 |
| Co1 | +1.00606 |
| O1 | −0.37077 |
| O2 | −0.37602 |
| O3 | −0.35183 |
| O4 | −0.36630 |

| $PbNi_2(SeO_2OH)_2(SeO_3)_2$ | |
|---|---|
| atom | charge ± $q$ |
| Pb1 | +0.81193 |
| Pb2 | +0.82647 |
| Se1 | +0.27735 |
| Se2 | +0.27396 |
| Se3 | +0.28956 |
| Se4 | +0.28127 |
| Ni1 | +0.99233 |
| Ni2 | +0.96340 |
| O1 | −0.36194 |
| O2 | −0.35874 |
| O3 | −0.35630 |
| O4 | −0.35919 |
| O5 | −0.33540 |
| O6 | −0.35710 |
| O7 | −0.33391 |
| O8 | −0.35640 |
| O9 | −0.38723 |
| O10 | −0.35713 |
| O11 | −0.38634 |
| O12 | −0.35635 |
| H1 | +0.20398 |
| H2 | +0.20493 |

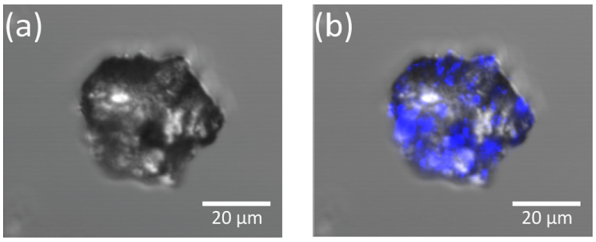


**Figure 7.** Transmission image of a crystal of $\beta$-$PbNi(SeO_3)_2$ (a); emitting surface ($\lambda_{em}$ = 420−440 nm, $\lambda_{em}$ = 860 nm), blue color (b).

anionic $(SeO_3)^{2-}$ and $(MO_6)^{10-}$ building units sharing common corners (Figure 3). We find one symmetrically independent $M^{2+}$ position with rather regular $(MO_6)^{10-}$ octahedral coordination. The average bonding ⟨M−O⟩ distances are 2.077 Å for **I** and 2.113 Å for **IV**. There are two independent Se atoms per formula unit where $Se^{4+}$ cations form typical $(SeO_3)^{2-}$ triangular pyramids with Se located at its apical corner and a stereoactive lone pair acting as a complementary external ligand. The average ⟨Se−O⟩ distance is 1.704 Å for both compounds, M = $Ni^{2+}$ (**I**) and $Co^{2+}$ (**IV**). The unique $Pb^{2+}$ site is surrounded by O anions shared by $(SeO_3)^{2-}$ and $(MO_6)^{10-}$ groups, forming asymmetric polyhedra. In both compounds the $Pb^{2+}$ cations demonstrate eight short strong Pb−O bonds (2.552−2.802 and 2.539−2.827 Å in **I** and **IV**, respectively) in one coordination hemisphere, and two longer weaker bonds (3.332 and 3.418 Å in **I** and **IV**, respectively) in the other hemisphere (Figure 4a,b) with a clear location of the stereochemically active lone pair. In Figure 3b a 3D metal cationic framework of the crystal structures of **I** and **IV** is represented as a black-and-white graph with black-and-white nodes symbolizing coordination polyhedra of $M^{2+}$ and $Se^{4+}$, respectively. It highlights the topological connectivity of the $SeO_3$ and $MO_6$ polyhedra in complex 3D framework with stretched rectangular channels extending along the [010] direction occupied by the lead cations and the $Se^{4+}$ lone pairs with a dimension of 3.1 × 11.4 $Å^2$, measured as the shortest and longest O···O distances across the channels (Figure 3b). In the (010) plane, their sections are arranged in a crossed manner with alternate of the two orientations [201] and the [20$\bar{1}$] with respect to the *Pnma* symmetry. The channels are bordered by six $MO_6$ and six $SeO_3$ polyhedra (Figure 3a). The projection of the channel walls is given in the figure resulting in a three M-octahedra-wide pseudoribbons (Figure 5a). Within the pseudoribbon, there are void spaces that are bounded by six-membered rings with a dimension of 5.35 × 5.46 $Å^2$. The pseudoribbons are further cross-linked into a 3D $[M(SeO_3)_2]^{2-}$ framework through common $SeO_3$ trigonal pyramids (Figure 5b). Divalent lead cations reside in the cavities and balance the charge of the framework of compounds **I** and **IV**. In general, it is typical for heteropolyhedral frameworks in inorganic oxysalts to be based upon interconnecting chains oriented parallel to each other.[32] The framework topology found out for $\alpha$-$PbM(SeO_3)_2$ (M = $Ni^{2+}$ and $Co^{2+}$) has been observed previously, e.g., in the structures of $(H_3O)[Fe(HPO_4)_2]$,[33] $Na_3[In(PO_4)_2]$,[34] and $Pb[Fe(AsO_4)(AsO_3OH)]$.[35]

***β*-PbNi(SeO$_3$)$_2$.** The crystal structure of **II** adopts an orthorhombic symmetry (noncentrosymmetric space group, $Cmc2_1$). It contains one symmetrically independent $Ni^{2+}$ cation that forms a slightly distorted $NiO_6$ octahedron: the trans O−Ni−O bond angles fall in the range of 155.82−172.69°, whereas the cis angles range from 80.91° to 102.94°. The Ni−O bond lengths are 2.045(5)−2.148(6) Å. Two independent $Se^{4+}$ sites have a trigonal pyramidal coordination with an apex occupied by the selenium cation as already mentioned previously. The average ⟨Se−O⟩ bond lengths of the trigonal pyramids are 1.698 and 1.707 Å for Se1 and Se2 sites, respectively. In the crystal structure of **II** a unique $Pb^{2+}$ ion has seven short Pb−O bonds (2.569−2.885 Å) in the first coordination hemisphere, whereas the second hemisphere is occupied by two longer bonds (3.035 Å) (Figure 4c). Once again, the coordination polyhedra of the lead cation is asymmetric and obviously indicates that the $6s^2$ lone pair is stereochemically active. In contrast, we have recently described the crystal structure of $PbBi_4O_6Cl_2$ in which the $Pb^{2+}$ lone pair activity is fully quenched.[36]

Similarly to what was found in the $\alpha$-$PbNi(SeO_3)_2$ form (**I**), the $\beta$-form is built up from isolated $NiO_6$ octahedra interlinked by $SeO_3$ groups via common oxygen corners. However, the linkage modes differ in both structures. The crystal structure of **II** (Figure 6a) is essentially two-dimensional (2D) and is based upon $[Ni(SeO_3)_2]^{2-}$ sheets. They are shown in Figure 6b and lay parallel to (001). The lone pairs of electrons of $Se^{4+}$ cations are shifted in the [001] direction toward the vacant part of the interlayer space. The sheets in **II** are very similar to 2D pseudoribbons delimiting the channels of **I** and **IV**. Same cavities are filled by the $Pb^{2+}$ cations, which serve to balance charge and achieve the cohesion between the sheets. The shortest interlayer O···O contacts across the interlayer is about 3.36 Å, much greater than the sum of van der Waals radii and involves a true 2D-


DOI: 10.1021/ic503055v
*Inorg. Chem.* 2015, 54, 2425−2434

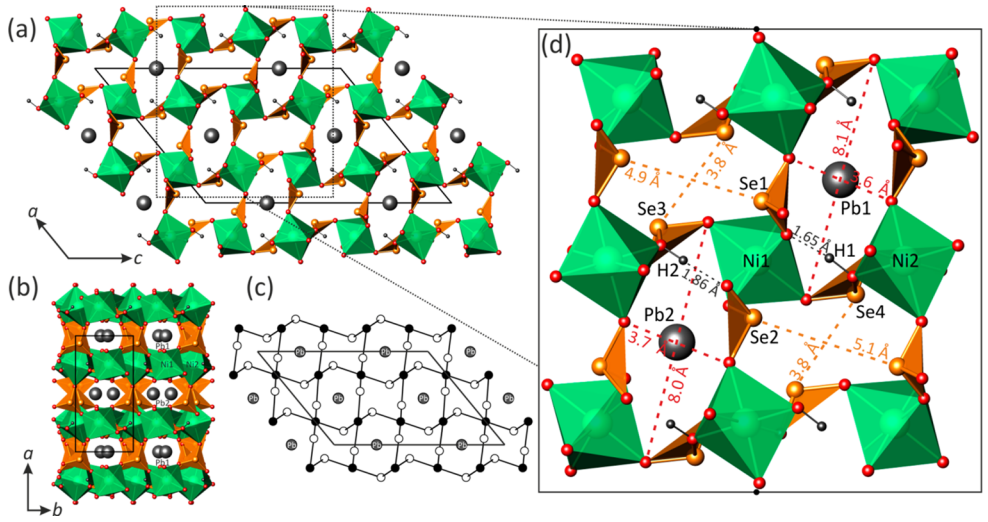


**Figure 8.** General projection of the crystal structure of $PbNi_2(SeO_2OH)_2(SeO_3)_2$ along the *b* and *c* axes (a and b), respectively; its black-and-white graph (c); and more detailed fragment of the structure (d). Legend as in Figure 4.

character. The black-and-white graph corresponding to the layered nickel selenite structural units is shown in Figure 6c. This kind of layer topology is one of the most common in inorganic oxysalts[32,37] and has been recently observed, for instance, in the crystal structure of steklite, $K[Al(SO_4)_2]$,[38] where $(AlO_6)$ octahedra are linked by $(SO_4)$ tetrahedra. In selenites, it has been reported for the crystal structures of $K_2[M(SeO_3)_2]$ (M = Mn and Co).[39,40] The NCS character of **II** is well evidenced on Figure 6a where only "*up*" $SeO_3$ orientations are found in the crystal structure. Dipole moments were calculated for **II** due to its noncentrosymmetricity. In this calculation performed using Pacha,[29] local charges given in Table 3 have been used. In general, it is noteworthy that the charge distribution is very similar in the four new selenites, due to similar concomitant groups. $Ni^{2+}$ and $Co^{2+}$ show a similar degree of covalence leading to a residual covalence charge close to ∼+1. As expected the Se−O bonds are very strong leading to a residual charge around +0.25. Finally, the shortest Pb−O distances also bring a strong degree of covalence leading to Pb partial charge close to +1. For **II**, all $SeO_3$ groups stand in to bring local dipole moments that do not cancel each other. The moments are mainly oriented along the [001] direction with values of 1.87 and 2.07 Debyes for $Se(1)O_3$ and $Se(2)O_3$, respectively. Other local dipoles arise from distorted $NiO_6$ octahedra and $Pb^{2+}$ complex coordination polyhedra that also lead to a net nonzero polarization due to the $Cmc2_1$ symmetry. Finally each individual layer shown on Figure 6a brings its own total dipole, mainly parallel to *c* but with different (*a*, *b*) components. Our calculations performed on the $[Pb_4Ni_4(SeO_3)_8]$ unit-cell content containing two layers lead to *M* = 21.51 Debyes almost parallel to *c* (negative charge barycenter (1.157, −0.111, 2.197), positive charge barycenter (−1.189, −0.256, −1.617)). This important value is expected to lead to strong SHG effects. Our analysis was performed on three different crystals of **II** as detailed in the Experimental Section. Dealing with a rather thick crystal, only some areas of the crystal surface show a significant SHG signal as shown in blue color in Figure 7. This feature is rather common and was observed recently in $[Bi_{12}O_{15}][Li_2(SO_4)_4]$.[41] It is noteworthy that in the experimental setting the detected SHG signal is maximal in the horizontal plane (below the crystal), which reduces the detection for thick and irregular absorbing samples In addition the refinement of racemic twinned domains (ratio ∼ 60:40) suggests the possibility for local SHG quenching at the antiphase boundary.

**Polymorphism in $PbNi(SeO_3)_2$.** In our experiments, we have observed two modifications of $PbNi(SeO_3)_2$ that differ in both crystallographic parameters and structural topology. The *α*-phase has a notably smaller unit-cell volume (544.83 $Å^3$) than the *β*-phase (575.81 $Å^3$) and, as a consequence, a remarkably higher density (6.337 versus 5.996 $g/cm^3$, respectively). In terms of structural complexity expressed as a Shannon information amount per unit cell,[42,43] the *β*-phase is considerably more simple (58.439 bits per unit cell) than the *α*-phase (116.877 bits per unit cell). It is a general observation that a high-temperature polymorph is structurally simpler than its low-temperature counterpart (due to the increase in both vibrational and configurational entropies),[44] which, together with the data on density and unit-cell volumes, strongly suggest that the *α*- and *β*-modifications of $PbNi(SeO_3)_2$ are low- and high-temperature polymorphs, respectively. This conclusion agrees well with the 3D and 2D characters of their structures, respectively, which is frequently observed in inorganic compounds (that is, structural dimensionality of a low-temperature polymorph is higher than that of its high-temperature counterpart[45]).

**$PbNi_2(SeO_2OH)_2(SeO_3)_2$.** The crystal structure of **III** adopts a monoclinic symmetry (space group, *P*2/*c*). There are two symmetrically independent $Ni^{2+}$ sites with rather regular octahedral coordination with the average ⟨Ni−O⟩ bond lengths equal to 2.064 and 2.077 Å for Ni1 and Ni2 sites, respectively. The four crystallographically inequivalent $Se^{4+}$ atoms are asymmetrically coordinated by three oxygen atoms in a trigonal pyramidal geometry. However, two of them are protonated leading to strongly distorted $(Se(3)O_2OH)^-$ and $(Se(4)O_2OH)^-$ trigonal pyramids with one long Se−O bond (1.810 and 1.785 Å for Se(3) and Se(4), respectively) and two shorter Se−O bonds (1.659−1.676 and 1.649−1.675 Å for Se3 and Se4, respectively). Similarly distorted coordination geometry is typical of hydroxide ligands, as reported for instance in the crystal structure of $Ni(HSeO_3)\cdot 4H_2O$.[46] The average ⟨Se−O⟩ bond lengths are equal to 1.695, 1.693, 1.715, and 1.703 Å for $Se(1)O_3$, $Se(2)O_3$, $Se(3)O_2OH$, and $Se(4)O_2OH$, respectively. The two independent $Pb^{2+}$ cations are 8-fold oxygen coordinated (Figure 3d,e) with Pb−O distances in the ranges of 2.481−2.916 and 2.567−2.765 Å for Pb1 and Pb2, respectively. They both



DOI: 10.1021/ic503055v
*Inorg. Chem.* 2015, 54, 2425−2434

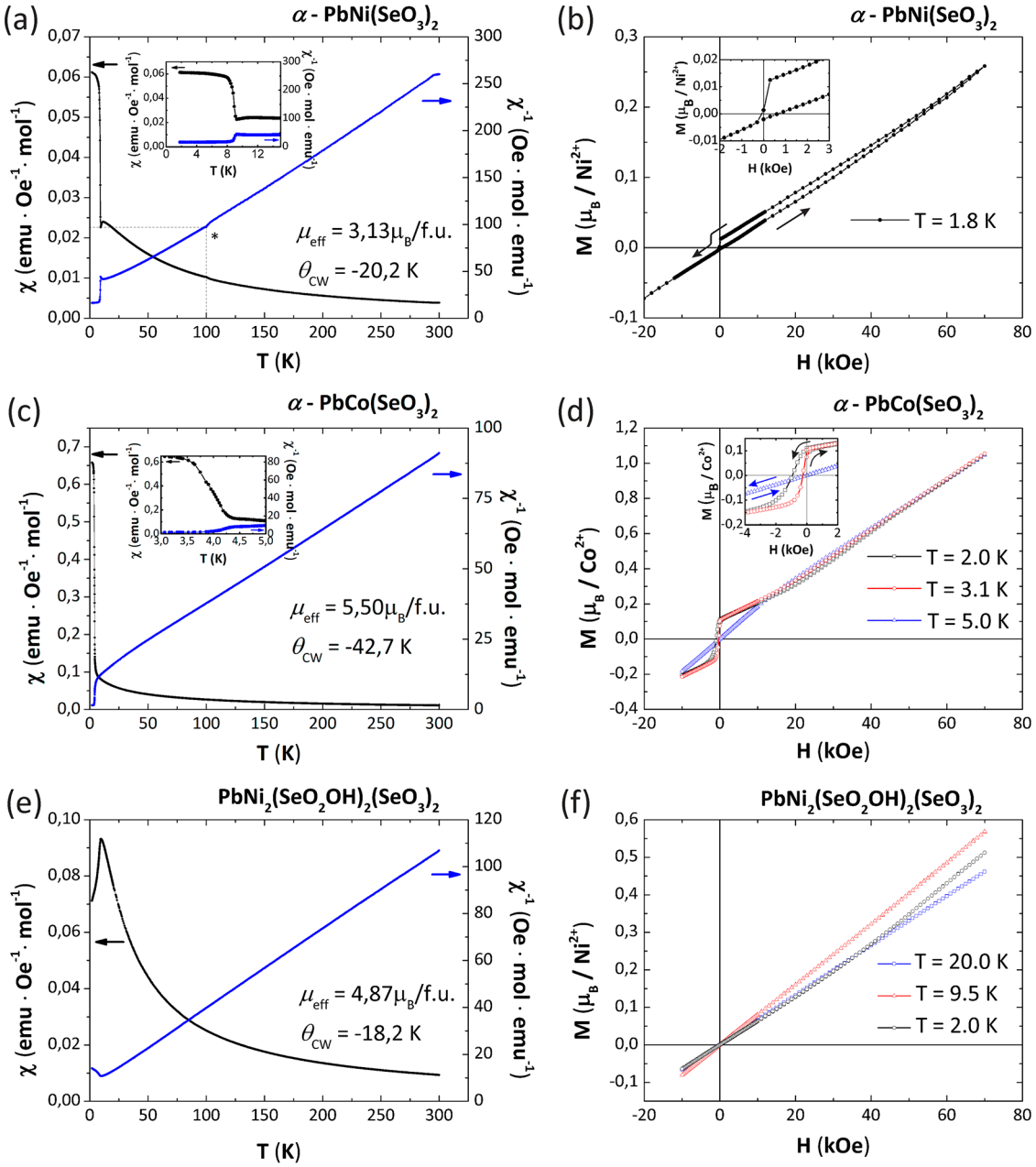


**Figure 9.** Thermal evolution of the magnetic susceptibility for **I** (a), **IV** (c), and **III** (e). Magnetization as a function of applied field for **I** (b), **IV** (d), and **III** (f).

show a distorted square antiprismatic arrangement with lone pairs of electrons oriented toward the longest oxygen neighbors, similarly to lead coordination in $PbMo_2O_5(SeO_3)_2$.[10]

In the crystal structure of **III**, the $NiO_6$ octahedra are sharing their vertices with $SeO_3$ groups, forming a 3D framework encapsulating channels propagating along the [010] direction (Figure 8a). Four independent channels are occupied alternately by divalent lead cations and lone pairs of electrons of the $Se^{4+}$ cations. The channels containing $Pb^{2+}$ are bordered by $O^{2-}$ ions and have a cross-section of maximum of ~3.6 × 8.1 Å$^2$ taking into account the shortest O···O separations. Those bordered by $Se^{4+}$ ions Se···Se are ~3.8 × 5.1 Å$^2$ large on the basis of the Se···Se distances (Figure 8d). It is striking that in the (*a*,*b*) projection the similitude between Pb1 and Pb2 channels suggests a *V*/2 subcell. In fact the projection in the (*a*,*b*) plane evidences channels growing along the *c*-axis with a clear distinction between Pb2 and Pb1 sites (Figure 8b).

Figure 8c shows the black-and-white graph corresponding to a 3D metal cationic framework of **III**. Its structural architecture is closely related to that observed in the crystal structure of $PbFe_2(SeO_3)_4$[47] and represents an interesting topological variation of the primitive cubic (pcu) network.[48]

## MAGNETIC PROPERTIES

The powder samples selected for magnetic measurements have been prepared from stoichiometries corresponding to the $P_1$ (**I** and **IV** (replacing NiO by CoO)) and $P_2$ (**III**) points in Figure 1a. After Rietveld refinement though strong preferred orientation effects, the refined phase weight fractions of impurity (diamagnetic $Pb(SeO_3)$) are 0.17, 0.42, and 0.15 for the powder samples of **I**, **III**, and **IV**, respectively. Magnetic data were


DOI: 10.1021/ic503055v
Inorg. Chem. 2015, 54, 2425−2434

normalized taking into account the massic contribution of the second phase. PXRD patterns are shown in Figure 2.

The FC magnetic susceptibility $\chi$ and $\chi^{-1}$ versus temperature are plotted in Figure 9a,c for $\alpha$-$PbNi(SeO_3)_2$ (**I**) and $\alpha$-$PbCo(SeO_3)_2$ (**IV**). In the high-temperature range, $\chi^{-1}(T)$ could be fitted using a Curie–Weiss law $\chi = C/(T - \theta_{CW})$. Both compounds show very similar behavior dominated by antiferromagnetic exchanges as given by the negative Curie–Weiss temperatures, $\theta_{CW} = -20.2$ and $-42.7$ K, respectively. The deduced effective moments are 3.13 $\mu_B$ and 5.50 $\mu_B$ per formula unit, respectively. It indicates significant spin–orbit couplings (SOC) compared to calculated spin-only values, i.e., 2.83 $\mu_B$/$Ni^{2+}$ and 3.87 $\mu_B$/$Co^{2+}$. One should also note that the exaggerated value measured in the cobalt compound compared to the commonly observed $\mu_{eff} \sim 4.5$ $\mu_B$ probably denote an approximate determination of the **IV** compound's weight fraction in the biphasic sample, due to preferred orientation effects mentioned previously.

For **I** the broad peak below 100 K and the upturn of the susceptibility below 9 K suggests the setting of short-range antiferromagnetic correlations but is immediately masked by the appearing of a magnetic moment. In **IV** a similar, but even more abrupt, phenomenon occurs below 4.5 K. In both compounds, it is accompanied by a ZFC/FC divergence at low temperature, as shown in Supporting Information Figure S12. It is ascribed to intrinsic spin-canting due to favored antisymmetric exchanges (Dzyaloshinski–Moriya interactions) in this crystal structure with strong SOC ions. As expected from the strongest SOC for $Co^{2+}$, the M(H) magnetization plot indicates a largest remanent moment for **IV** compared to **I**, i.e., 0.1 $\mu_B$/$Co^{2+}$ against 0.01 $\mu_B$/$Ni^{2+}$ as shown on the Figures 9b,d. In the mean-field approximation, the Curie–Weiss temperature is given as $\theta_{CW} = 2zJS(S+1)/3k_b$ where the $z$-number of neighbors interact with the same $J$ force with a central $M^{2+}$ ion. Theoretically, this approximation is available in the Heisenberg case but could lead to an approximated value for $Co^{2+}$ and $Ni^{2+}$ ions where spin–orbit coupling should favor anisotropic spins ($XY$ or Ising).

Dealing with similar crystal structures of **I** and **IV**, one can derive $J_{(I)}/J_{(IV)} = \theta_{CW(I)}(S_{Co^{2+}})(S_{Co^{2+}} + 1)/\theta_{CW(IV)}(S_{Ni^{2+}})(S_{Ni^{2+}} + 1) = 0.89$. This involves very similar $J$ coupling values. Taking into account that each metal center is surrounded by z = 8 other metals with plausible M–O–O–M superexchange paths (4.8 Å < M–M < 6.2 Å and O–O distance smaller than the sum of their ionic radii), one can also estimate the mean $J$ value to $J/k_b \sim -1.9$ and $-2.1$ K, respectively.

$\chi(T)$ and $\chi^{-1}(T)$ of compound **III** are shown on Figure 9e. It shows a paramagnetic regime above the setting of an antiferromagnetic transition at $T_N = 10$ K. The Curie–Weiss law above $T_N$ yields $\mu_{eff} = 4.87$ $\mu_B$/(formula unit (f.u.)). (3.44 $\mu_B$/$Ni^{2+}$) and $\theta_{CW} = -18.2$ K in good agreement with predominant antiferromagnetic exchanges between $Ni^{2+}$ ions with strong SOC. Once more, in a mean-field approximation can we deduce a mean $J_{Ni-Ni}/k_b$ of $-1.71$ K from the $\theta_{CW}$ value, taking into account $z$ equals eight Ni neighbors around each $Ni^{2+}$ with efficient geometrical SSE paths under conditions given previously. This low value is nearly similar to the one found for compound **I** and gives an indication for weak but comparable Ni–O–O–Ni negative exchanges mediated by $SeO_3$ corners in both compounds.

## CONCLUSION

In this work, the PbO–NiO–$SeO_2$ ternary system in hydrothermal conditions at 473 K was investigated. Three novel lead nickel selenites and one novel lead cobalt selenite were synthesized and characterized. The $PbNi(SeO_3)_2$ compound crystallizes in two polymorphic orthorhombic modifications, $\alpha$ (**I**) and $\beta$ (**II**). The $PbCo(SeO_3)_2$ phase (**IV**) is isotypic with **I**. According to the experimental results, the pH values of the solution play the essential role in hydrolysis and condensation processes by hydrothermal reactions in the studied system and determine structural architectures of resulted products of the syntheses. The observed dependence of the structural variety and the structural units upon the pH values is remarkable and can be used for preparation of new transition metal oxoselenites and similar groups of heavy-element compounds with novel structural architectures.

## ASSOCIATED CONTENT

### Supporting Information

Tables listing fractional atomic coordinates, atomic displacement parameters, and selected bond distances, figures showing experimental XRD patterns and temperature dependences of magnetization, and crystallographic information files. This material is available free of charge via the Internet at http://pubs.acs.org.

## AUTHOR INFORMATION

### Corresponding Author

*E-mail: olivier.mentre@ensc-lille.fr.

### Notes

The authors declare no competing financial interest.

## ACKNOWLEDGMENTS

This work was carried out under the framework of the Multi-InMaDe project supported by the ANR (Grant ANR 2011-JS-08 00301). The Fonds Européen de Développement Régional (FEDER), CNRS, Région Nord Pas-de-Calais, and Ministère de l'Education Nationale de l'Enseignement Supérieur et de la Recherche are acknowledged for funding the X-ray diffractometers. V.M.K. thanks l'Ambassade de France en Russie and l'Agence Campus France (Contract Nos. 768231K, 779116K, 794852B, 808399A, and 808400J) for the partial support of this work. S.V.K. and O.I.S. acknowledge financial support from St. Petersburg State University (Internal Grant 3.38.136.2014).

## REFERENCES

(1) Dadap, J. I.; Shan, J.; Heinz, T. F. *J. Opt. Soc. Am. B* **2004**, *21*, 1328–1347.
(2) Cady, W. G. *Piezoelectricity: An Introduction to the Theory and Applications of Electromechanical Phenomena in Crystals*; Dover Publications: New York, 1964; p 822.
(3) Jona, F.; Shirane, G. *Ferroelectric Crystals*; Pergamon Press: Oxford, U.K., 1962; p 402.
(4) Lang, S. B. *Sourcebook of Pyroelectricity*; Gordon and Breach Science: London, New York, 1974; p 562.
(5) Verma, V. P. *Thermochim. Acta* **1999**, *327*, 63–102.
(6) Effenberger, H. *J. Solid State Chem.* **1988**, *73*, 118–126.
(7) Li, P.-X.; Kong, F.; Hu, C.-L.; Zhao, N.; Mao, J.-G. *Inorg. Chem.* **2010**, *49*, 5943–5952.
(8) Yeon, J.; Kim, S.; Nguyen, S. D.; Lee, H.; Halasyamani, P. S. *Inorg. Chem.* **2012**, *51*, 609–619.
(9) Zhang, S.-Y.; Hu, C.-L.; Li, P.-X.; Jiang, H.-L.; Mao, J.-G. *Dalton Trans.* **2012**, *41*, 9532–9542.
(10) Oh, S.; Lee, D. W.; Ok, K. M. *Inorg. Chem.* **2012**, *51*, 5393–5399.
(11) Oh, S.-J.; Lee, D. W.; Ok, K. M. *Dalton Trans.* **2012**, *41*, 2995–3000.


DOI: 10.1021/ic503055v
*Inorg. Chem.* 2015, 54, 2425–2434

(12) Kovrugin, V. M.; Colmont, M.; Mentré, O.; Siidra, O. I.; Krivovichev, S. V. *Mineral. Mag.* **2015**, submitted for publication.
(13) Kovrugin, V. M.; Siidra, O. I.; Colmont, M.; Mentré, O.; Krivovichev, S. V. *Mineral. Petrol.* **2015**, submitted for publication.
(14) Aliev, A.; Kovrugin, V. M.; Colmont, M.; Terryn, C.; Huvé, M.; Siidra, O. I.; Krivovichev, S. V.; Mentré, O. *Cryst. Growth Des.* **2014**, *14*, 3026−3034.
(15) Vlaev, L. T.; Genieva, S. D.; Gospodinov, G. G. *J. Therm. Anal. Calorim.* **2005**, *81*, 469−475.
(16) Forster, P. M.; Stock, N.; Cheetham, A. K. *Angew. Chem., Int. Ed.* **2005**, *44*, 7608−7611.
(17) Sonnauer, A.; Stock, N. *Eur. J. Inorg. Chem.* **2008**, *2008*, 5038−5045.
(18) Engelen, B.; Bäumer, U.; Hermann, B.; Müller, H.; Unterderweide, K. *Z. Anorg. Allg. Chem.* **1996**, *622*, 1886−1892.
(19) Wildner, M. *Monatsh. Chem.* **1991**, *122*, 585−594.
(20) Mcmanus, A. V. P.; Harrison, W. T. A.; Cheetham, A. K. *J. Solid State Chem.* **1991**, *92*, 253−260.
(21) Amorós, P.; Marcos, M. D.; Roca, M.; Beltrán-Porter, A.; Beltrán-Porter, D. *J. Solid State Chem.* **1996**, *126*, 169−176.
(22) Popovkin, B. A.; Cheremisinov, V. P.; Simanov, Y. P. *J. Struct. Chem.* **1963**, *4*, 38−43.
(23) Fischer, R. *TMPM, Tschermaks Mineral. Petrogr. Mitt.* **1972**, *17*, 196−207.
(24) Koskenlinna, M.; Valkonen, J. *Cryst. Struct. Commun.* **1977**, *6*, 813−816.
(25) Pasero, M.; Rotiroti, N. *Neues Jahrb. für Mineral., Monatsh.* **2003**, *2003*, 145−152.
(26) *APEX*; Bruker AXS: Madison, WI, USA, 2007.
(27) *SADABS*; Bruker AXS: Madison, WI, USA, 2001.
(28) Sheldrick, G. M. *Acta Crystallogr.* **2008**, *A64*, 112−122.
(29) Henry, M. *ChemPhysChem* **2002**, *3*, 561−569.
(30) Pourbaix, M. *Atlas of electrochemical equilibria in aqueous solutions*; National Association of Corrosion Engineers: Houston, TX, USA, 1974; p 644.
(31) Takeno, N. *Atlas of Eh-pH diagrams*, Geological Survey of Japan Open File Report No.419; National Institute of Advanced Industrial Science and Technology, Research Center for Deep Geological Environments: Tsukuba, Japan, 2005; p 287.
(32) Krivovichev, S. V. *Structural Crystallography of Inorganic Oxysalts*; Oxford University Press: Oxford, U.K., 2009.
(33) Vencato, I.; Mattievich, E.; Moreira, L. F.; Mascarenhas, Y. P. *Acta Crystallogr.* **1989**, *C45*, 367−371.
(34) Lii, K.-H. *Eur. J. Solid State Inorg. Chem.* **1996**, *33*, 519−526.
(35) Effenberger, H.; Hejny, C.; Pertlik, F. *Monatsh. Chem.* **1996**, *127*, 127−133.
(36) Aliev, A.; Olchowka, J.; Colmont, M.; Capoen, E.; Wickleder, C.; Mentré, O. *Inorg. Chem.* **2013**, *52*, 8427−8435.
(37) Krivovichev, S. V. *Crystallogr. Rev.* **2004**, *10*, 185−232.
(38) Murashko, M. N.; Pekov, I. V.; Krivovichev, S. V.; Chernyatyeva, A. P.; Yapaskurt, V. O.; Zadov, A. E.; Zelensky, M. E. *Geol. Ore Deposits (Transl. of Geol. Rudn. Mestorozhd.)* **2013**, *55*, 594−600.
(39) Wildner, M. *Acta Crystallogr.* **1992**, *C48*, 595−595.
(40) Wildner, M. *Acta Crystallogr.* **1992**, *C48*, 410−412.
(41) Lü, M.; Colmont, M.; Huvé, M.; De Waele, I.; Terryn, C.; Aliev, A.; Mentré, O. *Inorg. Chem.* **2014**, *53*, 12058−12065.
(42) Krivovichev, S. V. *Acta Crystallogr.* **2012**, *A68*, 393−398.
(43) Krivovichev, S. V. *Angew. Chem., Int. Ed.* **2014**, *53*, 654−661.
(44) Krivovichev, S. V. *Mineral. Mag.* **2013**, *77*, 275−326.
(45) Krivovichev, S. V.; Cahill, C. L.; Burns, P. C. *Inorg. Chem.* **2002**, *41*, 34−39.
(46) Engelen, B.; Boldt, K.; Unterderweide, K.; Bäumer, U. *Z. Anorg. Allg. Chem.* **1995**, *621*, 331−339.
(47) Johnston, M. G.; Harrison, W. T. A. *J. Solid State Chem.* **2004**, *177*, 4680−4686.
(48) Krivovichev, S. V. *Mineral. Mag.* **2014**, *78*, 415−435.


DOI: 10.1021/ic503055v
*Inorg. Chem.* 2015, 54, 2425−2434